TECHNICAL PAPER

Hybrid deposition additive manufacturing: novel volume distribution, thermo-mechanical characterization, and image analysis

Muhammad Harris[1,2] · Hammad Mohsin[3] · Johan Potgieter[1] · Khalid Mahmood Arif[4] · Saqib Anwar[5] · Abdullah AlFaify[5] · Muhammad Umar Farooq[6]

Abstract

The structural integrity of additive manufacturing structures is a pronounced challenge considering the voids and weak layer-to-layer adhesion. One of the potential ways is hybrid deposition manufacturing (HDM) that includes fused filament fabrication (FFF) with the conventional filling process, also known as "HDM composites". HDM is a potential technique for improving structural stability by replacing the thermoplastic void structure with a voidless epoxy. However, the literature lacks investigation of FFF/epoxy HDM-based composites regarding optimal volume distribution, effects of brittle and ductile FFF materials, and fractographic analysis. This research presents the effects of range of volume distributions (10–90%) between FFF and epoxy system for tensile, flexure, and compressive characterization. Volume distribution in tensile and flexure samples is achieved using printable wall thickness, slot width, and maximum width. For compression, the printable wall thickness, slot diameter, and external diameter are considered. Polylactic acid and acrylonitrile butadiene styrene are used to analyze the brittle and ductile FFF structures. The research reports novel application of image analysis during mechanical characterization using high-quality camera and fractographic analysis using scanning electron microscopy (SEM). The results present surprising high tensile strain (0.038 mm/mm) and compressive strength (64.5 MPa) for lower FDM-percentages (10%, 20%) that are explained using in situ image analysis, SEM, stress–strain simulations, and dynamic mechanical analysis (DMA). In this regard, the proposed work holds novelty to apply DMA for HDM. The optimal volume distributions of 70% and 80% alongside fractographic mechanisms for lower percentages (10%, 20%) can potentially contribute to structural applications and future material-based innovations for HDM.

Keywords Fused filament fabrication · Additive manufacturing · Mechanical characterization · Dynamic mechanical analysis · In situ image analysis · Scanning electron microscopy · Hybrid deposition manufacturing

---

Technical Editor: Zilda de Castro Silveira.

✉ Muhammad Harris
m.harris@massey.ac.nz; engr.harris@uet.edu.pk

Hammad Mohsin
hmohsin1@gmail.com

Johan Potgieter
j.potgieter@massey.ac.nz

Khalid Mahmood Arif
k.arif@massey.ac.nz

Saqib Anwar
sanwar@ksu.edu.sa

Abdullah AlFaify
aalfaify@ksu.edu.sa

Muhammad Umar Farooq
mn21muf@leeds.ac.uk

[1] Massey Agrifood (MAF) Digital Labs, Massey University, Palmerston North 4410, New Zealand

[2] Industrial and Manufacturing Engineering Department, Rachna College of Engineering and Technology, Gujranwala 52250, Pakistan

[3] Polymer Engineering Department, National Textile University, Faisalabad 37610, Pakistan

[4] Department of Mechanical and Electrical Engineering (SF&AT), Massey University, Auckland 0632, New Zealand

[5] Industrial Engineering Department, College of Engineering, King Saud University, PO Box 800, Riyadh 11421, Saudi Arabia

[6] School of Mechanical Engineering, University of Leeds, Leeds, UK

Springer

1 Introduction

Fused filament fabrication (FFF), also known as fused deposition modeling (FDM) has become the trademark technology in additive manufacturing (AM) [1–3]. Ease of access, low cost of materials and 3d printers are the highlights that make FFF a common choice for domestic and commercial users [4]. The research for FFF is reported in various domains: materials [5, 6], process optimization [7], feeding mechanism (filament [4], pellets [8]), and large-scale additive manufacturing [9–14]. Large-scale additive manufacturing using FFF is one of the challenging processes nowadays. In this regard, researchers add carbon fibers to achieve the desired mechanical properties and printability [12]. However, the overall cost ends too high due to expensive carbon fibers alongside insufficient mechanical properties [15].

The pronounced reasons for insufficient mechanical properties are weak layer-to-layer adhesion [16, 17], and an inherent void-based structure of FFF [18, 19]. Various researchers present different processing parametric combinations for improving the layer-to-layer adhesion and reducing the voids. Sharma et al. [20] investigated the effects of infill density, layer thickness, and printing speed on the mechanical properties of FDM samples. The reported results reveal highest effect of 92% in elongation and 80% in tensile stress followed by layer thickness and printing [20]. Alafaghani et al. [21] presented a detailed work on effects of processing parameters on mechanical properties, building time, and dimensional accuracy. The processing parameters of building direction, infill density, infill pattern, layer thickness, printing speed, and printing temperature are investigated [21]. The research concludes infill percentage as one of the decisive factor [21]. Vaezi et al. [22] present the extrusion-based AM for Polyether ether ketone (PEEK) at different processing parameters. A significant effect of infill density is reported in form of 14% and 31% porosity for samples printed with 100% and 80% infill densities [22]. Therefore, the literature shows the infill density as one of the significant processing parameters along with others [20–22]. Furthermore, the literature reveals the inherited weakness in form of voids even with 100% infill density that resulted notable changes in mechanical properties [20–22].

Considering the importance of infill percentage, majority researchers adopted 100% infill to maintain the uniformity with literature and to carter the variable porosity (in percent) associated with different infill percentages [23–25]. This results in non-optimized use of extra material that results waste in terms of material, cost, time and efforts [26, 27]. In this regard, an aspect of design optimization is reported by various researchers [26–29]. The proposed work in design optimization is mostly related with allocation of material in maximum stress vicinities within overall design using CAD and simulation-based software [26, 29]. The allocation of material in particular areas instead of printing complete part helps to avoid redundant 3d printing and hence results in less material utilization, time, and cost [26]. Apart from optimization of material utilization in specific areas, the literature reports 20–100% infill to 3d print the remaining optimized design [30]. This reaches the same problem of having porosities, even at 100% infill density, in the printed part despite being optimized in design.

Considering the complexity associated with void formation, it is important to understand the mechanism of void formation that depends upon the shape of extruded bead [31]. There are numerous reasons behind managing shape of extruded bead which can be categorized in two categories, i.e., processing parametric variations, and material properties [31]. The latter is quite rare as the material properties (viscosity) are optimized before 3d printing to achieve optimal extrusion. However, the material is vulnerable to show high expansion along with randomly oriented beads due to low viscosity that may lead to variable void density [32]. On the other hand, the processing parameters are majorly encountered by users as the main reason for void formation. The effective processing parameters causing variation in voids formation and density are speed, feed, layer height (thickness), infill density, infill pattern, number of outer perimeters, nozzle temperature, ambient temperature etc. [7, 20, 26, 32–35]. For example, the higher the speed, thinner will be the bead; the lower the feed, lower will be the bead size; the larger (coarse) the layer height, the larger will be the bead; the lower the infill density, the smaller and farther will be the bead; the lower the nozzle temperature, the more round will be the bead; the lower the ambient temperature, the more round will be the bead. All before mentioned cases results in high void formation and thus produces high void density [7, 20, 26, 32–36]. The large void density results in high losses in mechanical properties (tensile, compression, and flexure) [32]. Recent research also reveals the quality of 3d printer, particularly open source 3d printer, to be one of the valid reasons for variable void density [30, 37]. The lack of accuracy between X, Y, and Z axis movements due to substandard stepper motors, lead screws, and stop sensors results in variable accuracy in different prints [8, 37]. Therefore, it highlights a need to explore different ways to overcome high void density.

A logical solution to these problems is the replacement of void-based structure/part with a dense structure. Fortunately, one of the unique additions in additive manufacturing is the combination of FFF with different additive [38] and subtractive processes [39], also known as hybrid additive manufacturing. The simplest of hybrid additive manufacturing is the

fill compositing [40], also known as hybrid deposition manufacturing (HDM) composite [41], which includes the FFF printing followed by deposition or filling with polyurethane or epoxy binary system [41]. The filled material potentially serves the purpose of a non-void or dense structure that can help to achieve better structural integrity, particularly considering the scope of large scale-structures in this research.

To the best of our knowledge, literature reports rare articles on filled FFF structures [40, 41]. Raymond et al. [41] deposits the polyurethane in 3d-printed robotic actuators with different design strategies (hooks, locking voids) lacking flexure characterization. Furthermore, the research lacks the analysis of standardized samples (ASTM or ISO) [41] to evaluate the real strength of proposed HDM parts. Joseph et al. [40] performs the flexure characterization of epoxy filled FFF samples lacking tensile characterization. Therefore, the facts depict that HDM composites are not yet extensively researched. Furthermore, the literature lacks the information regarding following key aspects: (1) optimal volume distribution between FFF and filled polymer resins, (2) stability to tensile, compressive, flexure, and fatigue loadings, (3) in situ analysis of fracture propagation during mechanical testing, (4) post-mechanical testing fracture analysis, and (5) comparison of the effects of brittle and ductile FFF materials on structural stability during the application of external load.

This research presents, a detailed novel analysis for a range of volume distributions between FFF material (polylactic acid-PLA and acrylonitrile butadiene styrene-ABS) and two-part epoxy in light of mechanical characterization (tensile, compressive, flexure, and fatigue). The in situ monitoring of mechanical characterization is performed for analyzing the true nature of fracture using high-quality image recording. Furthermore, post-destructive fractographic analysis at the microscopic level using scanning electron microscopy (SEM) is performed to analyze the nature of the fracture. The research provides optimal volume distributions for the standardized samples of tensile, compressive, flexure, and fatigue based on obtained numerical results and the nature of the fracture. The research work also presents a logical reasoning for the in-depth interpretation of unusual mechanical results, that are not being found and presented yet. Overall, the research provides a logical means to evaluate the feasibility of HDM composites to be used for structural applications.

2 Materials and methods

2.1 Materials

PLA and ABS filaments of 1.75 mm diameter are procured from Prusa and Stratasys, respectively. White color is selected based on optimal properties attained in literature [42]. The specific gravity of PLA and ABS are 1.24 g/cm^3 and 1.05 g/cm^3, respectively. The glass transition temperature (T_g) of PLA and ABS are 55–60 °C and 105 °C, respectively. The recommended printing temperatures by corresponding suppliers are 210 °C for PLA and 272 °C for ABS. The supplier provided strength at break for PLA and ABS is 50 MPa and 25 Mpa, respectively.

Two-part west epoxy 105 and hardener 206 is purchased from industrial fiberglass solutions, New Zealand. The pot life of 105/206 epoxy system is 20–25 min. The epoxy system takes 10–15 h to cure into solid.1–4 days to gain working strength. Minimum recommended temperature for curing is 16 °C. The reported supplier maximum viscosity is 725 cps as per ASTM D2393 at 22.2 °C.

A new PRUSA i3 MK3S 3d printer is procured from PRUSA RESEARCH, UK for this research to avoid any component-based inaccuracies in build quality.

2.2 Methods

2.2.1 Fabrication of HDM samples

The HDM samples are fabricated in three stages: (1) 3d printing of slotted FFF parts, and (2) pouring epoxy/hardener system into FFF-printed slots, (3) curing and deaeration of hybrid samples in vacuum. Figure 1 shows the stages.

The first stage includes the preparation of CAD drawings for slotted FFF parts on Solidworks for tensile, compression, and flexure samples. The drawings are installed in "stl" format followed by slicing on "Prusa Slicer version 2.2.0" software. Prusa Slicer converts the "stl" drawings into G-codes that are printed using a PRUSA i3mk3S 3D printer. The FFF printing is performed using polylactic acid and acrylonitrile butadiene styrene. The 3d printer is monitored within a tolerance of + 0.05 mm during experimentation. It is further explained in Sect. 2.2.2.

The second stage includes the preparation of Epoxy/hardener. The epoxy to hardener ratio by 5:1 by parts. Both resin and hardener are properly mixed manually with each other with a stirrer in a simple bowl and poured into FFF-printed samples. The pouring process is performed manually with proper care using a pipette. Special care is taken for avoiding formation of air bubbles during pouring. The pouring is performed in PC2 Lab of Massey University, where the lab temperature is maintained in range of 20–25 °C.

The third stage includes the deaeration of incomplete HDM samples for removal of entrapped air bubbles. The deaeration is performed in a vacuum desiccator using a suction pump. The removal of air bubbles is performed at room temperature maintained in range of 20–25 °C. The vacuum suction of air bubbles is carried for 3–5 h. The desiccating
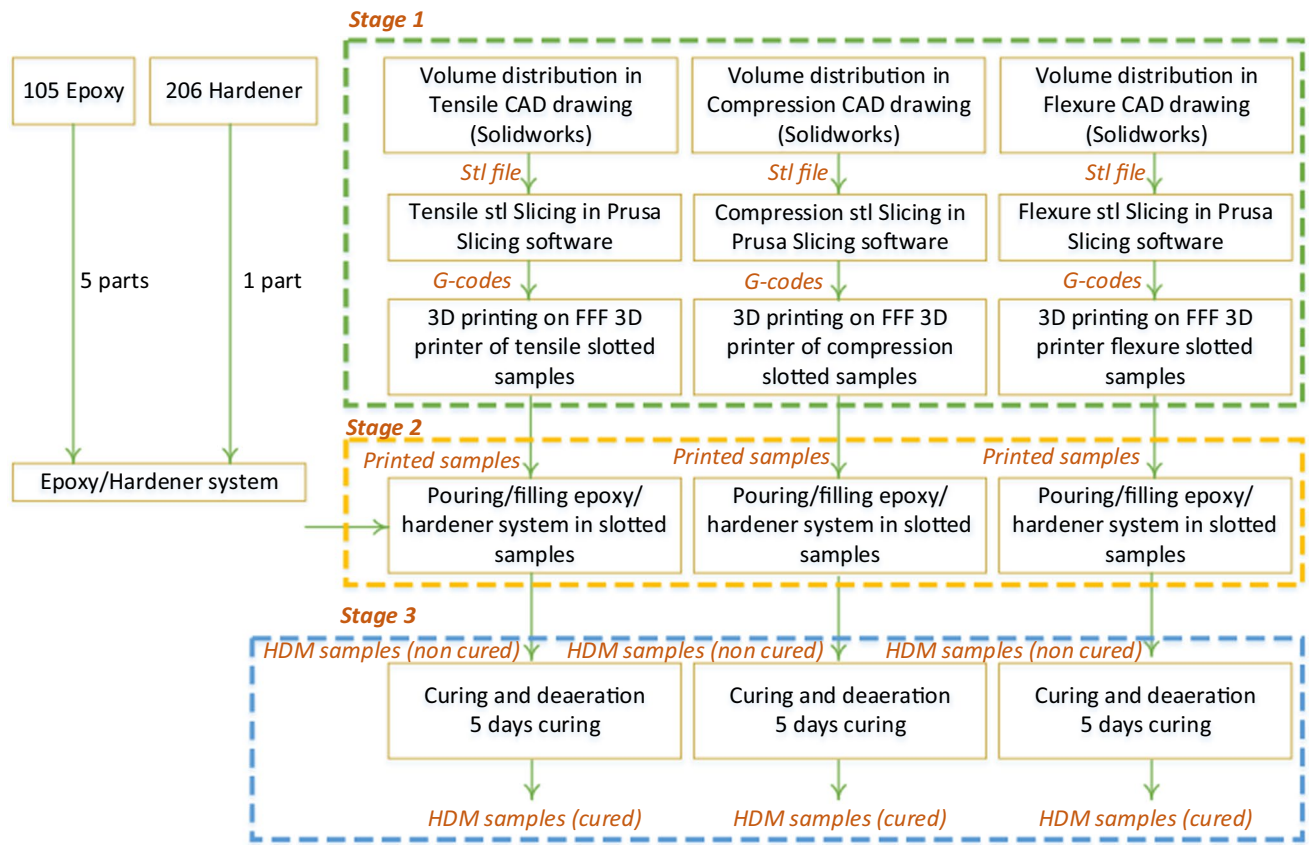
Fig. 1 Stages of manufacturing a HDM composite in this research

Table 1 Volume distribution in tensile specimens

Volume percentage of FFF	Width of gauge length (mm)	Gauge length (mm)	Thickness (mm)	Distance between grips (mm)	Wall thickness of one side (≤ 2.9) (mm)	Volume of 100% FFF between grips (mm^3)	Volume of slot between grips (mm^3)	Comments
10	6	33	4	65	0.32	2241.86	228.37	Not possible. Too thin to print
20	6	33	4	65	0.67	2241.86	447.06	Possible
30	6	33	4	65	1.00	2241.86	661.86	Possible
40	6	33	4	65	1.35	2241.86	885.75	Possible
50	6	33	4	65	1.73	2241.86	1119.36	Possible
60	6	33	4	65	2.10	2241.86	1343.25	Possible
70	6	33	4	65	2.47	2241.86	1566.03	Possible
80	6	33	4	65	2.87	2241.86	1800.61	Possible
90	6	33	4	65	3.20	2241.86	2017.2	Not possible. > 6 mm width

process is followed by drying in open environment at room temperature (20–25 °C) for 5 days.

2.2.2 3d printing and volume distribution

Fused filament fabrication is performed for three types of characterizations (tensile, compressive, flexure) using following parameters: layer thickness 0.2 mm, width 0.4 mm, infill density 100%, fill angle 90°, perimeter speed 45 mm/sec, infill speed 80 mm/sec, infill perimeter overlaps 100%, extruder temperature 210 °C, bed temperature 60 °C, extrusion multiplier 1, and build orientation flat (XY). The printing is performed on polyether imide (PEI) plate on PRUSA i3MK3S 3d printer without using any tape. Minimum of 3 samples are printed for each combination given in Tables 1, 2 and 3. One sample is printed at a time for each of tensile, compression, and flexure.

The method for volume distribution is calculated using simple mathematical relation shown in Fig. 2d. The slicing software is used to calculate the total volume of 100% FFF samples (tensile, compression, flexure). The wall thickness is then adjusted using slicing software, for example, Fig. 2d

shows that the 50% of 100% FFF is 1601.71 mm^3 that is 49.77% of the volume of 100% FFF (3217.59 mm^3).

The tensile specimens are made as per the ASTM D638 type IV [43, 44] standard based on the optimal mechanical properties. The volume distribution is performed with respect to the volume between the grips (Fig. 2 and Table 1). The volume inside the grips is not included in the volume distribution calculations (Table 1).

Furthermore, these samples do not have any inter-locking mechanism to grip epoxy and to impart uniform forces as reported for non-standardized samples [41]. Therefore, the slot containing epoxy is extended into the area of grips on both sides for 10 mm. The extension will impart equal gripping forces between epoxy and 3d-printed sections to maintain the uniform loading during tensile testing. "Prusa slicer" is used to slice the printing parts using 100% infill density with a rectilinear infill pattern and raster orientation in the direction of tensile load (90°). Prusa slicer does not have option to achieve same layer pattern in all successive layer. For example, using 90° will lead to 3d printing of 90/0 orientation throughout the height of the part. To achieve the linear (rectilinear) printing of beads in

Table 2 Volume distribution in flexure specimens

Volume percentage of FFF	Outside Width in of FFF (mm)	Thickness (mm)	Length between grips (mm)	Wall thickness of one side (mm)	Width of the slot (mm)	Volume of 100% FFF between grips (mm^3)	Volume of slot in FFF between grips (mm^3)	Comments
10	10	4	65	0.55	8.9	3200	325	Possible
20	10	4	65	1	8	3200	640	Possible
30	10	4	65	1.5	7	3200	960	Possible
40	10	4	65	2	6	3200	1280	Possible
50	10	4	65	2.5	5	3200	1600	Possible
60	10	4	65	3	4	3200	1920	Possible
70	10	4	65	3.5	3	3200	2240	Possible
80	10	4	65	4	2	3200	2560	Possible
90	10	4	65	4.5	1	3200	2880	Possible

Table 3 Volume distribution in compressive specimens

Volume percentage of FFF	External Diameter	Wall thickness (mm)	Internal diameter of the hole (mm)	Volume of 100% FFF (mm^3)	Volume of the FFF wall	Comments
10	12.5	0.44	12.06	3217.59	316.12	Possible
20	12.5	1.17	11.33	3217.59	656.75	Possible
30	12.5	1.90	10.6	3217.59	976.11	Possible
40	12.5	2.6	9.9	3217.59	1282.08	Possible
50	12.5	3.5	9.0	3217.59	1601.71	Possible
60	12.5	4.45	8.05	3217.59	1924.84	Possible
70	12.5	5.5	7.0	3217.59	2240.09	Possible
80	12.5	6.8	5.7	3217.59	2569.45	Possible
90	12.5	8.5	4.0	3217.59	2898.41	Possible

Fig. 2 Schematic and real images for Sample dimensions, infill pattern, and volume distribution in **a** Tensile (ASTM D638), **b** flexure (ISO 178), and **c** compression (ISO604)

Shape, dimensions, and 3D printing settings

(a)

(b)

(c)

Method for volume distribution

Volume of solid cylinder (100% FFF) = 3217.59 mm3

Adjust the wall thickness in CAD software to achieve 50% volume of 100% FFF

By hit and trial, at wall thickness of 3.5 mm

Volume of hollow cylinder is 1601.71 mm3

Using following relation,

=Volume of hollow CAD/ volume of 100% FFF cylinder

1601.71/3217.59= 49.77≈ 50%

(d)

the direction of applied force, the number of outer perimeters is increased to large number (25). The large number of perimeters helps to complete the part with perimeters only as shown in Fig. 2.

The flexure samples are designed as per ISO 178 [45]. The volume distribution is performed with respect to the "slot width" as shown in Fig. 2 and Table 2. Flexure samples are printed with 100% infill and linear raster orientation (90°).

The compressive samples are made according to the ISO 604 [46]. The volume distribution is performed with respect to the volume between outside and inside diameter as shown in Fig. 2 and Table 3. The linear infill pattern is used with 100% infill density for each sample.

2.2.3 Mechanical testing

The tensile testing is performed on Instron 5967 machine. The tensile characterization is performed at an extension rate of 5 mm/minutes. The machine is operated with a 30 kN load cell and a clip-on-gauge extensometer. The clip-on-gauge extensometer is used to measure the tensile extension and strain.

Flexure testing is performed on Instron 5967 using 3-point bending accessories. The 3-point bending testing is performed at an extension rate of 5 mm/min. The distance between the grips is 65 mm as shown in Fig. 2.

Compression testing is also performed on Instron 5967 machine using compression testing attachments. The test is conducted at an extension rate of 5 mm/min.

2.2.4 In situ image analysis

The High-speed monochromatic camera of 5 MPa is used for recording the images during mechanical testing. The camera is from Point Grey Machine Vision with 28 mm Sigma Aspherical Lens (KIPON, 1:1.8D EX DG). The software used to capture and process the pictures is Flycaputre version 2 (2.11.3.121) from FLIR integrated Imaging solutions, Inc. The diffused lights are used to preserve the details in shadows normally formed between beads at the surfaces of printed parts. The in situ image recording was performed at 1 frame per second (fps). The image analysis is used to obtain real-time information regarding mechanical transformations between different percentages of the polymer–polymer interface in HDM composite. Furthermore, it is used to investigate the flow of cracks and the nature of fracture in the samples.

2.2.5 Scanning electron microscopy (SEM)

SEM is used for the fractographic analysis of tensile and flexure samples performed on Hitachi TM3030 Plus. As the images are of good quality, so the samples are not coated with any material. The analysis is performed at various resolutions ranging from 1 mm to 300 μm (10×–300×). The main objectives of using SEM are to analyze the following: (1) nature of the fracture, and (2) effect of epoxy system on printed beads in from of cracks, bulging or sagging.

2.2.6 Dynamic mechanical analysis (DMA)

The DMA testing was performed on a TA Instruments' DMA Q800 (TA Instruments, New Castle DE, USA) using a single cantilever clamp in Multi-Frequency- Strain mode at 1 Hz and 20 μm from 25 to 130 °C. The available frequency mode on machine is multi frequency. Therefore, to achieve the purpose of single frequency testing, the frequency is set to a constant of 1 Hz.

The heating rate for all DMA scans was 5 °C/min. Rectangular specimens had the dimensions of 17.53 mm × 12.34 mm × 6.27 mm (length × width × thickness). DMA device is controlled by "Thermal Advantage software version 5.5.24". Storage modulus, tan delta, stress, and strain curves are obtained with respect to testing temperature range. These curves are analyzed in Universal Analysis software 2000 Version 4.5A.

3 Results

3.1 Tensile testing

The average ultimate tensile strength of PLA HDM in Fig. 3a shows a gradual increase with the increase in FFF volume. The results show the highest strength of 61.5 MPa for 80% samples, which is 6% higher than the reference sample (57.9 MPa). The average ultimate tensile strength (UTS) of 52 MPa and 54 MPa for 60% and 70%, respectively are also quite near to the reference samples making them feasible for consideration. The epoxy (0% sample) has the least average UTS, which presents the comparative effectiveness of incorporating epoxy into HDM composite. The strength of 61.8 MPa at 80% is equal to strength claimed for 100% infill samples in literature [47–49]. It is also notable that the
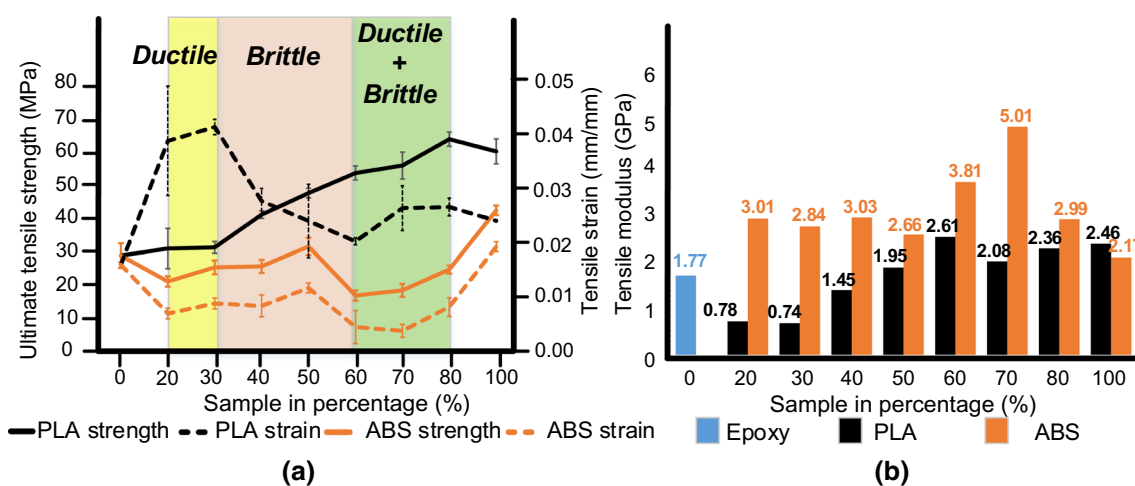
Fig. 3 Tensile properties: **a** average tensile strength (stress) vs average tensile strain, and **b** average tensile modulus

attained tensile strength for HDM PLA/epoxy composite is also comparable to injection mold sample [34].

The average tensile strain in Fig. 3a is too high at the beginning for 20% (0.038 mm/mm) and 30% (0.041 mm/mm) samples that keeps on decreasing steeply till 60% (0.019 mm/mm). It is noted that the average strain of 60% samples is even a bit less than the PLA reference (0.02356 mm/mm). However, the strain shows an increase thereafter for 70% (0.0258 mm/mm) and 80% (0.0261 mm/mm), that goes higher than the PLA reference (0.02356 mm/mm). The strain for the PLA/epoxy samples are more as compared to literature [34].

Based on the observed results, the compositions (20% and 30%) with high strain values are categorized as ductile compositions. With the steep decrease in strain for 40–60%, the compositions are categorized as brittle compositions. The last two compositions (70% and 80%) show recovery of strain, therefore, categorized as both ductile and brittle composites.

The volume distributions of 20–50% in Fig. 3b have less modulus than PLA reference that shows insufficient mechanical stability. Though the abovementioned strain is lowest for 60% with pronounced brittle effects of PLA, the increase in modulus from 60 to 80% shows better mechanical stability making these distributions feasible as an alternative to 100% PLA, especially 70% and 80% with comparatively high strength and strain.

ABS shows high incompatibility with the epoxy system as noted with low average UTS and strain at all distributions. The tensile modulus of ABS/epoxy HDM composite shows high peaks at all distributions as compared to the ABS reference because of extreme low strain. All samples are fractured early and thus failed to report good tensile strength. The early failure is described in "discussions". This depicts the poor mechanical stability of ABS/epoxy HDM composites.

3.2 Compressive testing

The compressive testing results similar proportional strength at 10% (64.52 MPa) and 20% (64.55 MPa) as like 100% PLA (65.9 MPa) (Fig. 4). Thereafter, the strength decreases till 40%, from where it climbs to a reasonable number around 50 MPa for 70% and 80%. The increase in strength after 40% depicts the overwhelming effects of PLA. However, the high strength at 10% and 20% is unexpected due to a thin layer of FFF structure and less individual strength of the epoxy system (Fig. 4). This requires special attention as it deviates from normal composite behavior. Therefore, it is complemented with detailed analysis in "discussions".

The strain in Fig. 4 is higher for 10%, 20%, and 30% as compared to the 100% PLA. However, the strain from 50 to 90% maintains itself at less than PLA reference, which shows high stability to compressive loads in the elastic region.

The proportional strength achieved at 70% and 80% ($\approx$50 MPa) in this work is comparatively high than reported in literature (20–50 MPa) [50, 51].

3.3 Flexure testing

The flexure strength and strain are shown in Fig. 5. For PLA, it is noted that the stress increases with the increase of volume distribution from 10 to 90%. Particularly, the samples with 40%, 50%, 60%, 70% 80% and 90% are far higher than the 100% PLA samples (reference). The strength of 40%, 50%, 60%, 70% 80% and 90% are 102.3 MPa, 112.6 MPa, 104 MPa, 109.2 MPa, 112.9 MPa, and 114.1 Mpa, respectively. The numbers achieved for 70%, 80% and 90% are higher than reported in literature (108 MPa) [52].

The strain of PLA/epoxy HDM composite is decreased as the volume distribution increase from 10 to 90%. The less strain with high stress at combinations above 40% shows
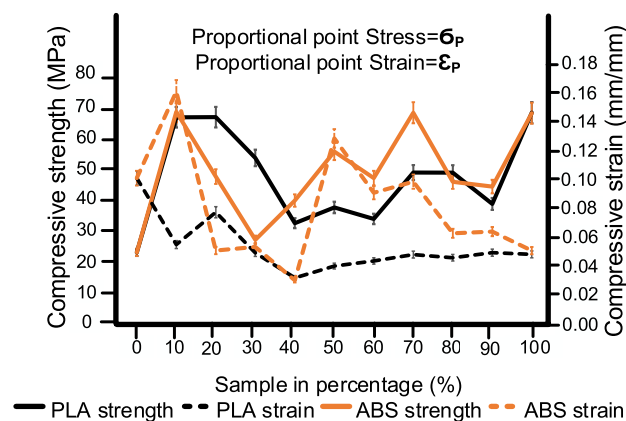
Fig. 4 Compressive properties of PLA and ABS-based HDM composites
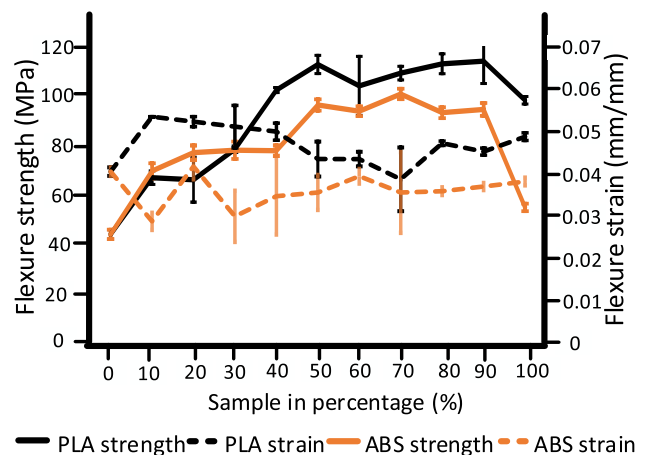
Fig. 5 Flexure properties of PLA and ABS-based HDM composites

high stiffness that proves the structural stability against flexure loading.

For ABS/epoxy HDM composite, there is an increasing trend of stress with increasing volume distributions. However, the PLA/epoxy HDM shows a significant increase in strength at most of the volume distributions as compared to the 100% ABS specimens.

Apart from 10 and 20%, the strain of ABS/epoxy HDM composite of all remaining distributions is close to the reference ABS. This may be due to the reason that pure epoxy and ABS have an almost similar strain that remains almost unchanged due to the understandable physical separation between two different materials. However, the combination of ABS with epoxy, even being dissimilar materials, in the form of a composite has helped to achieve significant strength.
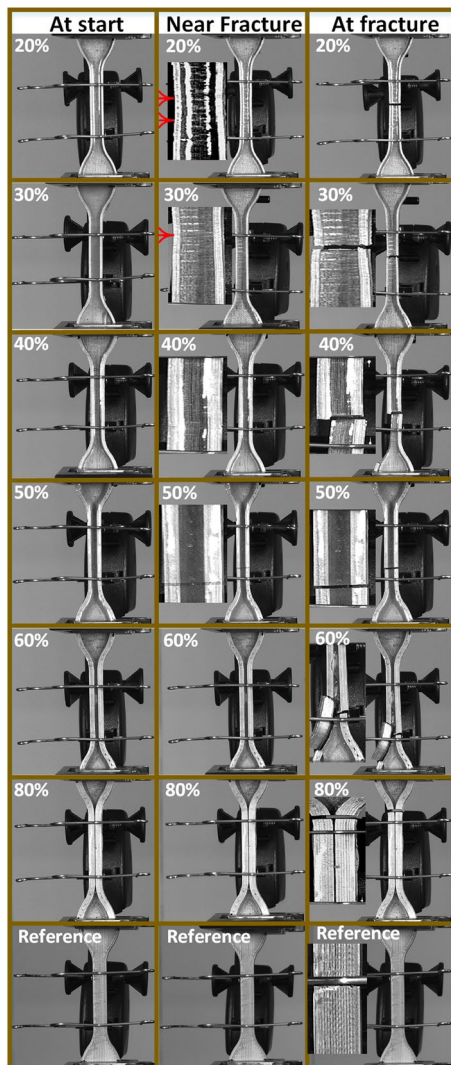
Fig. 6 In situ camera images for PLA/epoxy HDM tensile testing at different volume distributions

Further investigation of the relation between volume distributions is presented in the discussion.

4 Discussion

4.1 Analysis of tensile testing

The in situ images for PLA tensile testing of 20% and 30% show visible necking which is not found in PLA reference (Fig. 6). The specimens with 40% show minor necking, with one side (left) being more pulled than the other (right). The comparative more extension on one side leads to the chipping of a big piece of PLA off the epoxy after a fracture.

Another visible morphological change in Fig. 6 is the appearance of horizontal cracks in 20% and 30%. These horizontal cracks are observed to form due to the increase in tensile extension near the center of a dog bone. At a close look, the extension is actually noted for both PLA and epoxy system, that leads to cracks in the epoxy at stress concentrated volume. Besides the inward tilt as shown by red arrows in Fig. 6 for 20%, 30%, and 40%, the morphology of FFF is not expressive of the true facts for PLA-based HDM samples. Therefore, the fractographic analysis on scanning electron microscope (SEM) is performed in Fig. 7 separately.

The SEM analysis reveals the apparent reasons for: (1) tilt on one side (20%, 30%, and 40%), (2) necking, and (3) increasing strength with increase in volume distribution. Based on the observations, there are two factors that explain the overall tensile behavior of PLA/epoxy system: (1) adhesion of epoxy and (2) thickness of FFF structure.

Though the epoxy is a dissimilar material, it still appears to show sufficient adhesion to the immediate in-contact PLA perimeters/beads (Fig. 8). The sufficient physical adherence drags the internal PLA perimeters simultaneously with the increase in tensile force (Fig. 8). On application of tensile load, the epoxy in 20%, 30%, and 40%, as being in bulk volume, contracts from the upper half and expands in the lower half (Figs. 7 and 8). Thus, the upper half of FFF appears to contract along with the epoxy and expands at the lower half. During this contraction and expansion, it is observed that the elongation in each successive layer decreases with an increase in the number of printed vertical arrays (perimeters) away from the epoxy as shown in the schematic (Fig. 8). In the case of 20%, 30%, and 40%, there are fewer vertical arrays of beads (perimeters), therefore, the whole FFF wall is distorted with a visible tilt. This is prominent as wavy (distorted) surface beads at the outer surface of FFF as shown in column 3 and 4 of Fig. 7 for 20% and 30%. This is also a visible justification for the higher strains and necking at 20% and 30% observed in Fig. 3. As the perimeter thickness increase from 40 to 80% while decreasing the epoxy system volume, the strong intermolecular diffusion of PLA

Fig. 7 Scanning electron microscopy (SEM) analysis of PLA/epoxy HDM tensile specimens at the fractured cross section and outer side-ways beads
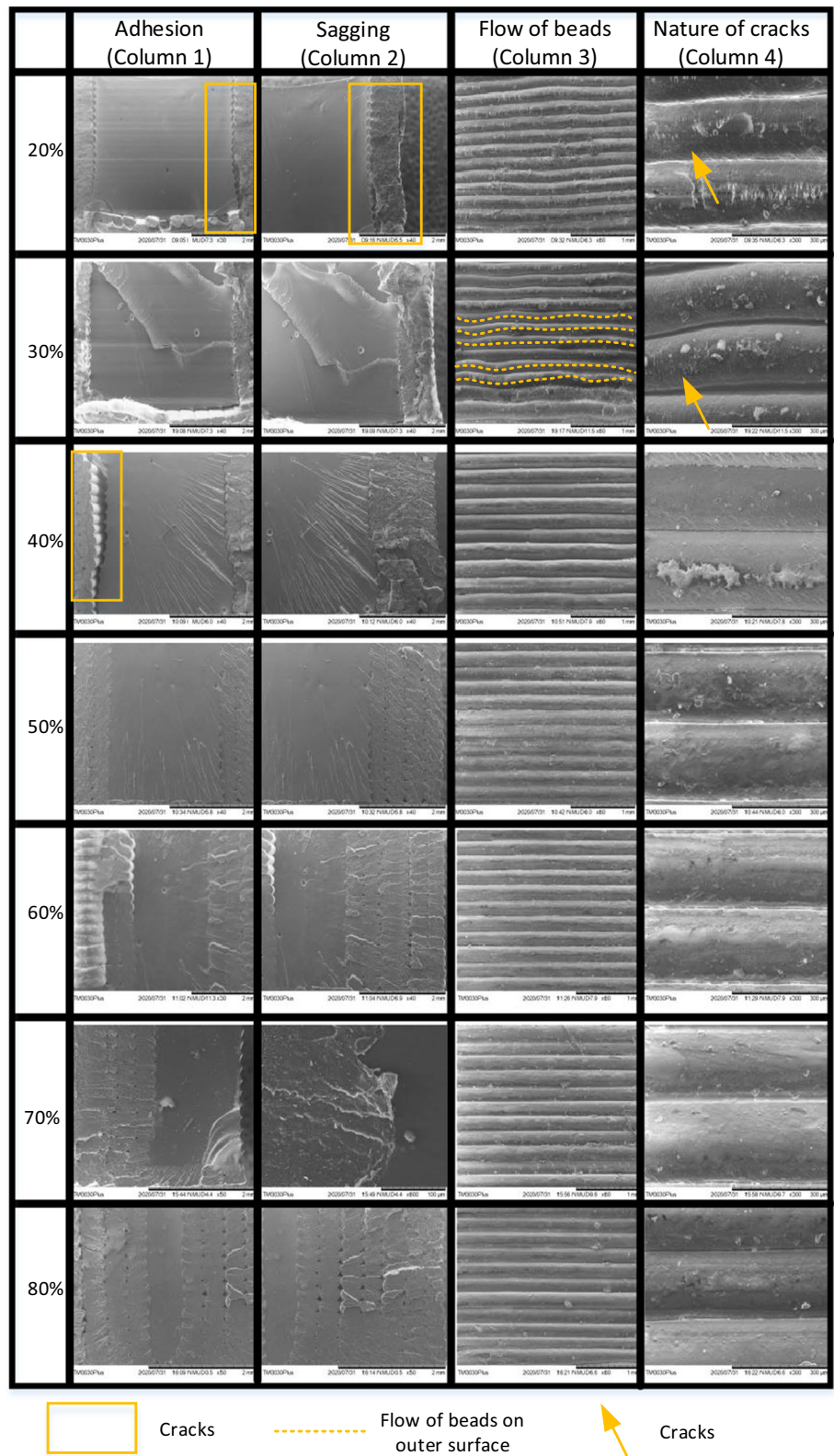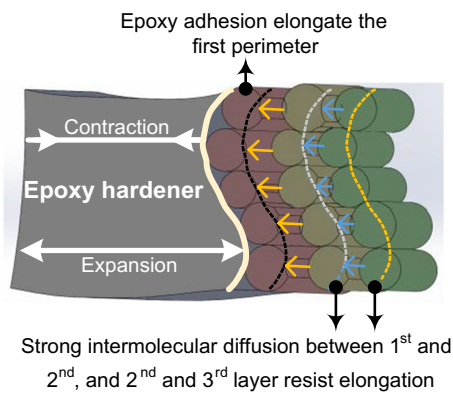
Fig. 8 Transfer of tensile forces from epoxy to outer-printed (FFF) layers in 20%, 30%, and 40% volume distributions based on observations
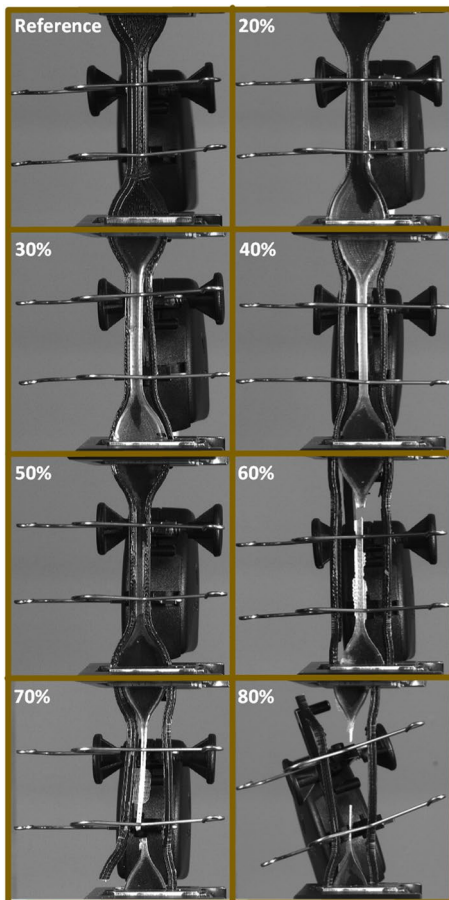
Fig. 9 In situ images for ABS/epoxy HDM composite samples at fracture

beads overcomes all structural distortions like contraction, expansion, and necking (Fig. 7). That is why there is no necking in samples from 50 to 80% along with less strain and high stress (Fig. 3a).

Furthermore, the vertical cracks at the surface of 20% and 30% also show the flow of tensile forces to the outermost layer, which are not found in the higher volume distributions (Fig. 7). This presents the reason for the high strength of higher volume distributions with less strain (higher modulus).

On the contrary, ABS composites with epoxy shows a separation of printed perimeters from epoxy system. This shows that the ABS and epoxy system are not compatible to make a composite HDM structure. This inability of ABS is an apparent reason for the less strength at all volume distributions of ABS/epoxy HDM (Fig. 9).

As shown in Fig. 9, the immediate separation of ABS from epoxy/hardener system reveals few important scientific facts. Though ABS registers weak chemical resistance to chlorinated solvents conditional to sufficient exposure time, i.e., atleast 3–4 months and suitable temperature [53]. However, the probable reason for non-adhesiveness is the non-reactiveness of ABS to epoxy/hardener system. The reactiveness is normally caused either after melting followed by degradation (scission) of intermolecular chains or gradual reaction of liquid-based solvents being in contact with ABS for sufficient long time periods (atleast 100 days) [54]. In this study, the non-reactivity is caused by couple of reasons, i.e., high melting point of ABS (170–200 °C), and less (insufficient) time of reaction between epoxy and hardener. The high melting point of ABS does not allow any initiation of chemical reaction of chlorinated epoxide groups. Similarly, the abrupt reaction of epoxy and hardener is the only source of producing high temperatures for initiating the reaction of ABS with epoxy resin. Unfortunately, the reaction time of epoxy and hardener is insufficient to initiate the reaction of chlorinated epoxy groups on ABS. The abovementioned reasons also highlights a new research proposition for making ABS reactive to epoxy/hardener system.

4.2 Analysis of compression testing

The compressive results for PLA in Fig. 4 show one of the highest compressive strengths for 10% and 20%. The highest strength probably designates 10% and 20% compositions as the strongest HDM compositions, even strongest than 90%. The thin FFF wall thickness of 0.5 mm in case of 10% and 0.69 mm in case of 20% raises serious questions regarding compressive endurance in elastic limit. Therefore, the analysis is extended beyond the proportional limit to the plastic region as shown in Fig. 10. Based on in situ images in Fig. 11, the second zone is named as bulk or sagging zone and the third zone is named as maximum load or crack zone.

The zone 2 is described with the lowest drop of compressive strength as marked in a Fig. 10 with the tangent. It is noted that the fast recovery with the least strain and less drop in strength helps to avoid sagging or bulking in the
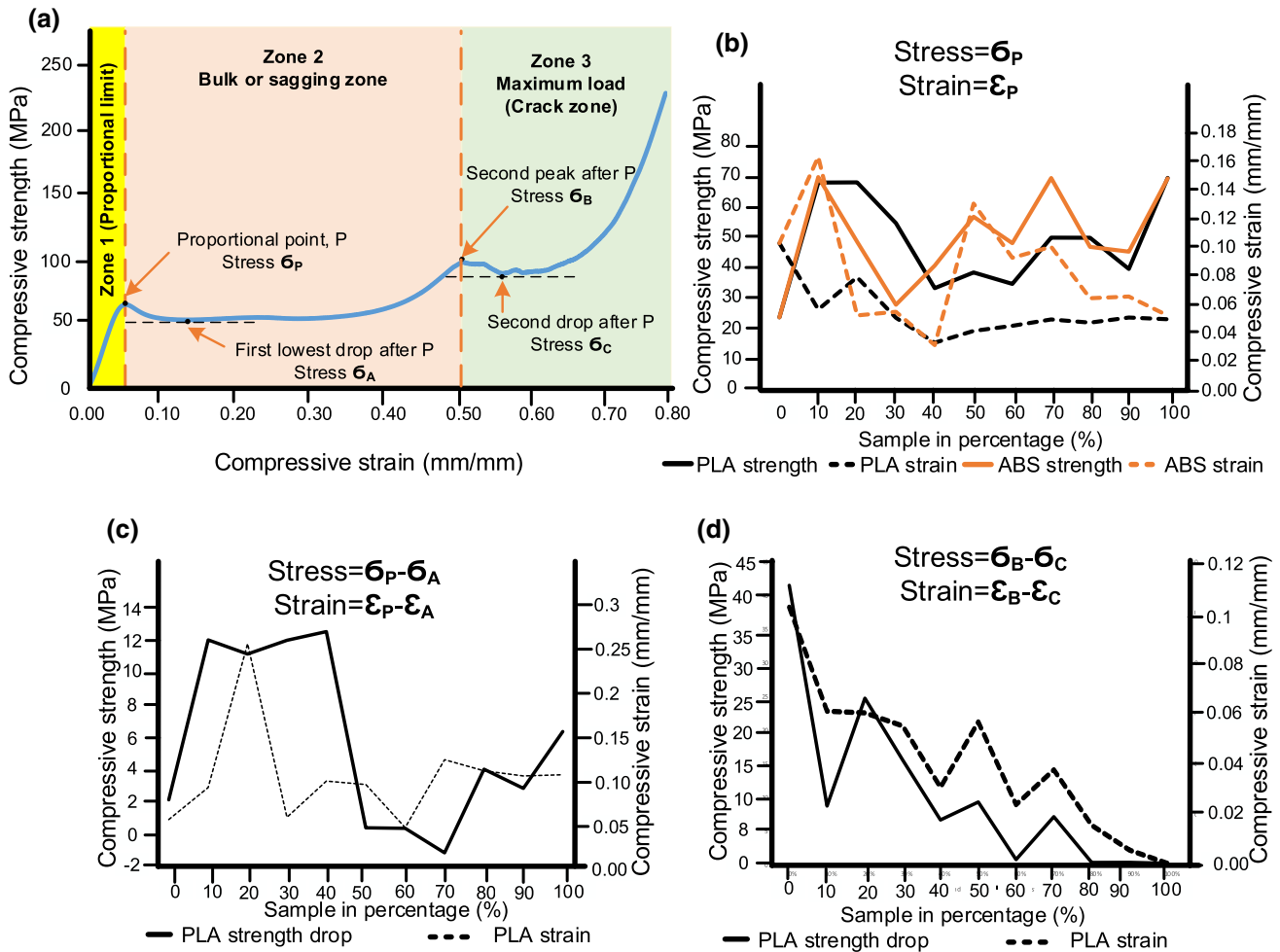
Fig. 10 Compressive properties: **a** stress–strain curve, **b** compressive stress up till proportional point, **c** stress drop after the proportional stress (first drop) w.r.t strain, and **d** the second drop in stress after the 2nd peak stress point w.r.t strain

middle zone. Figure 10c shows the difference of proportional point strength and lowest drop strength with corresponding compressive strain at the lowest drop point. It depicts that the stress difference is high for 10–40%, which decreases drastically from 50 to 80%. This shows that the highest proportional compressive strength of 10% and 20% is not the right presentation of the structure stability.

Zone three (3) is named after cracks observed in in situ images and at the highest load (30 kN). A similar kind of drop is noted in zone 3 as in Zone 2. However, as the volume distribution increases from 40% onwards till 100%, the graph reveals a low drop in strength with less strain. This also shows that the distributions below 40% are not mechanically feasible in terms of overall strength and strain.

Compressive samples are also analyzed using in situ images to investigate the unexpected results in Fig. 4. It is noted in Fig. 11 that the meager (thin) layer of FFF, at 10% and 20%, able to contain the epoxy in a close cylindrical volume that in turn shows high resistance to the compressive

forces. However, to achieve this unusual rise in stress, the upper part of the cylindrical structure is badly affected with the excessive bulge and highest compressive contraction length as shown in the 1st peak column of Fig. 11. This is also verified in FEA simulations (Fig. 12) in the form of the highest stress generated in the top plane of epoxy followed by FFF walls in 20%. Moving on, the structural stability is further compromised with severe non-uniform bulging at 1st drop within more compressive contraction. This structure instability is the reason for the highest 1st drop in the stress with high strain as found in results (Fig. 10c). Furthermore, the samples are noted with raptured 3d-printed PLA structure. The reason for the rapture is the high stresses in FFF walls of 20% as found in simulations (Fig. 12). Therefore, the image analysis and simulations at 1st stress peak, 1st drop, 2nd stress drop, and fracture highlights the instability of 10%, 20% and 30%.

On the contrary for 70%, 80%, and 90%, Fig. 11 shows a consistent decrease in the bulging of the upper part at
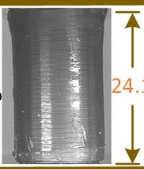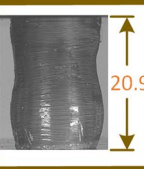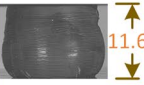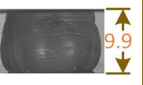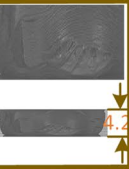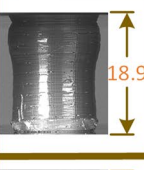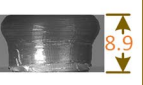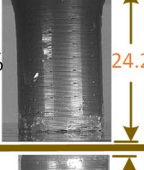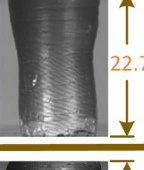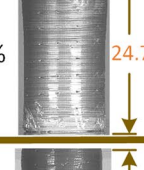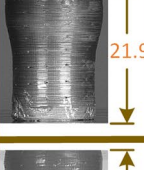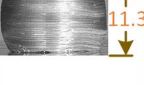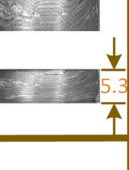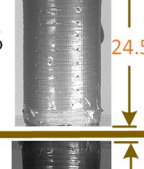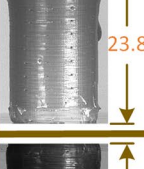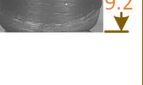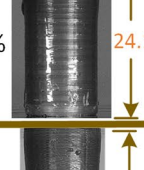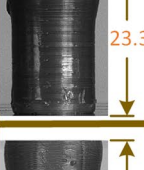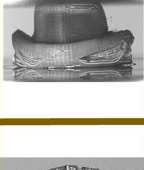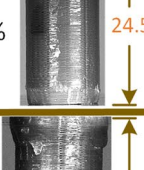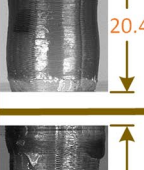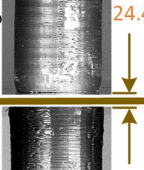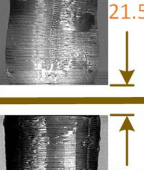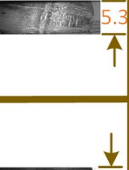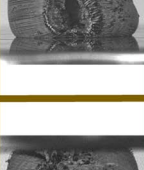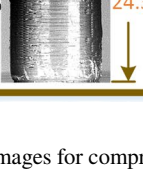
Fig. 11 In situ images for compressive testing of PLA/epoxy and ABS/epoxy HDM composites. All dimensions are in millimeters (mm)

Fig. 12 Compressive stress simulations for PLA/epoxy HDM composite at **a** 20% and **b** 80% samples

(a)   (b)
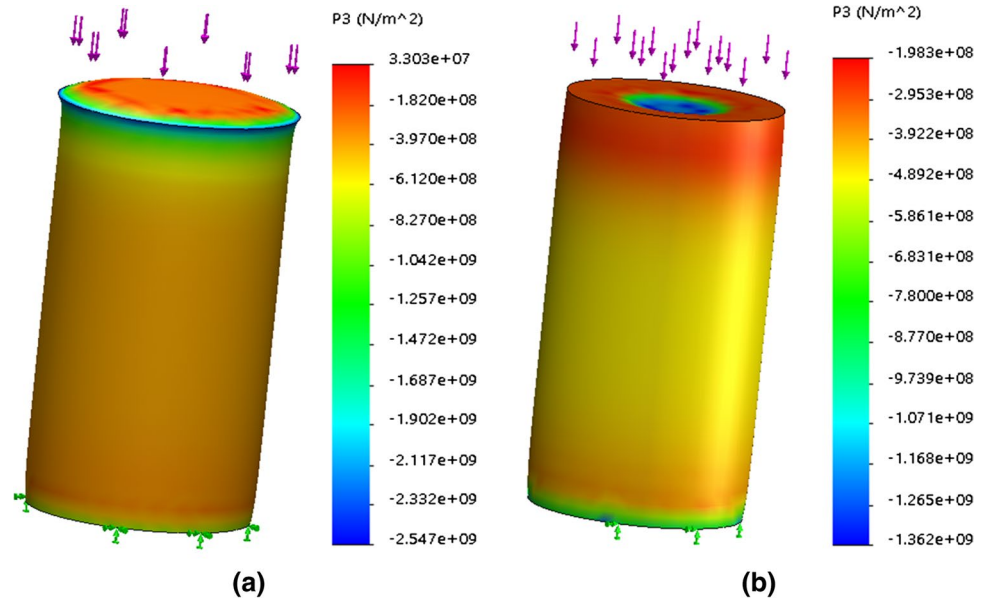
1st peak images with an increase in volume distribution. There are two reasons for this mechanical stability: (1) less epoxy volume causes less stress concentration in the top section, which avoids bulging that was significant in 10%, 20%, and 30% (Figs. 11 and 12), (2) sufficient the thickness of FFF structure to support the compressive load that bears the high stresses at the top section proficiently as shown in simulations (Figs. 11 and 12). The comparative less bulge at 1st peak stress is transformed into a uniform and controlled bulge profile at 1st drop that continues to provide consistent resistance to compressive load without any visible rapture at the fracture point. The high FFF percentage samples (70%, 80%, and 90%) are also observed less contraction at peak load of 30 kN as shown with more fracture height (Fig. 11). Therefore, this confirms the low strain at fracture in obtained compressive results (Fig. 10d) for 70–90%.

In compression, the ABS samples have high strength apparently than PLA/epoxy system HDM at most of the distributions (40–80%) as shown in Fig. 10b. However, the true picture is opposite to what the curves present in the results based on key findings in the in situ images. The distributions from 10 to 60% are observed with early fracture of ABS in the elastic zone (Fig. 11). The remaining higher distributions (70%, 80% and 90%) show some resistance to cracks in the elastic zone, but they are not able to keep their stability like similar distributions in PLA as noted in Fig. 11. This not only proves the instability of ABS as well as the effectiveness of using in situ images for analyzing the true characteristics of the HDM composites based on FFF material.
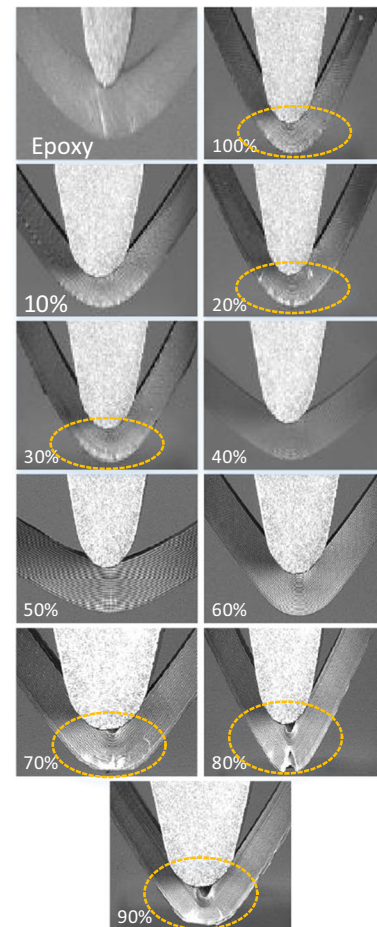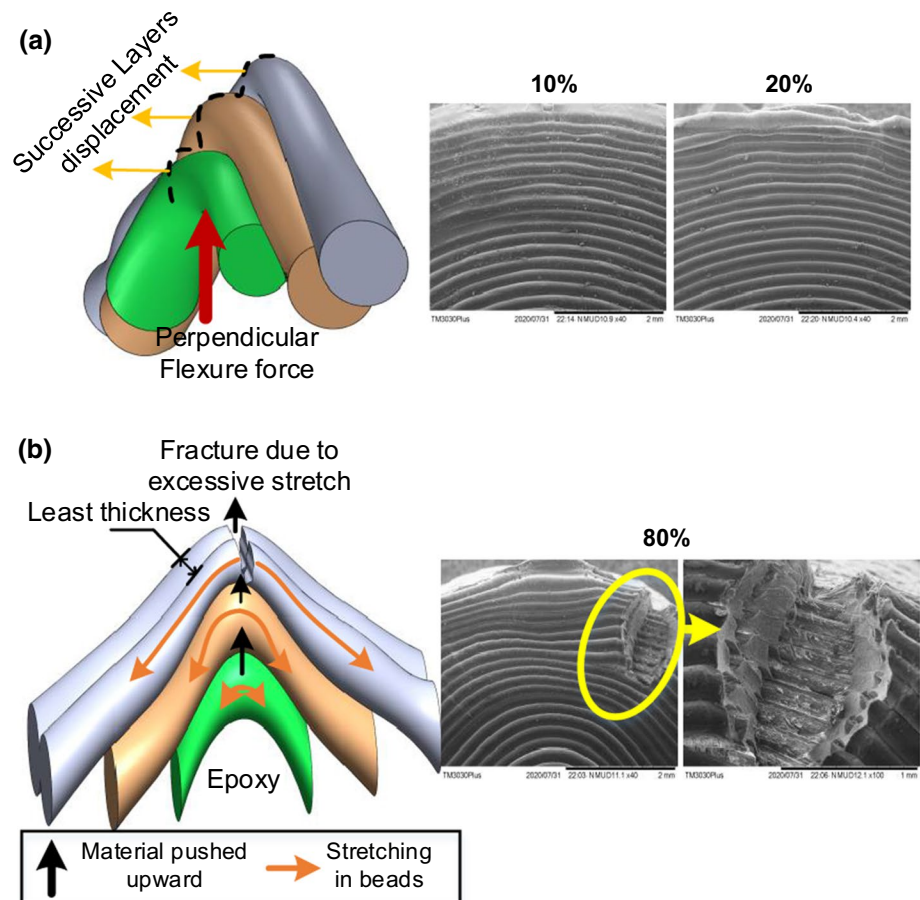

Fig. 13 In situ images for flexure testing of PLA/epoxy HDM composite specimens at the end of the test

Fig. 14 Scanning electron microscopy (SEM) analysis of FFF structure in flexure specimens of PLA/epoxy HDM composite

4.3 Analysis of flexure testing

In case of flexure, the results are not ambiguous like compressive. However, there are few important observations that help to validate the achieved results. For example, the majority of distributions of PLA/epoxy HDM have undergone excessive bending without having damage in the form of a break except for 40% and 50% (Fig. 13). Both distributions show the least bending to reach fracture (Fig. 13) that depicts an overwhelming brittle behavior of the HDM filling composite. Therefore, the high strengths of 102.3 MPa and 112.6 MPa for 40% and 50% respectively are not as reliable as of other higher distributions for PLA/epoxy HDM.

Another factor is noted for the effect of flexure forces on the thickness of the PLA FFF structure. As shown in the in situ images (Fig. 13), the cracks do not appear for lower distributions from 10 to 60%, and only appear for higher distributions (70%, 80%, and 90%). SEM is used to analyze the reason behind it. It is observed in Fig. 14 that the upper beads are displaced due to the perpendicular flexural forces. This is also because there are fewer adjacent layers to create sufficient adhesion between perimeters to resist the deformity in the upper structure. Therefore, the lack of perimeters in low volume distributions are not able to transfer complete flexure load uniformly to the lower part of FFF, thus displaced and avoid any cracks. However, in the case of higher distributions, the high number of adjacent layers (perimeters) perpendicular to the load keeps the beads intact, and hence no deformity is produced in the upper section as presented in the schematic (Fig. 14b). This strong adhesion increases the stretching of each successive bead to create a crack in the outermost layer as shown in Fig. 14b schematic and SEM analysis for 80% samples.

On the contrary, the ABS/HDM flexure samples show overall less strain at the outermost layers as all distributions are found with the crack (Fig. 15). This shows that ABS-based HDM composites are not ideal for practical applications. This again shows the impact of FFF material to be used as HDM composite material, that has not yet been reported.

4.4 Dynamic mechanical analysis

Dynamic mechanical analysis is used to investigate the low stress and high strain in low percentage samples (10%, 20%, and 30%). It is also used to justify the optimal percentage of the 3d-printed structure at an intermolecular level. The DMA analysis is only performed for PLA samples as the

Fig. 15 ABS/epoxy HDM composite samples after flexure testing. Note all are broken with minimum

ABS/epoxy HDM composites do not even show near-to-sufficient adhesion of FFF-printed ABS and filled epoxy resin in all mechanical characterizations. The poor adhesion results in abrupt disconnection or fracture of one or both FFF-printed ABS and filled epoxy resin. The disconnection or fracture results the purpose of combining both (ABS and epoxy) into one composite material and thus DMA will be able to provide true characteristic behavior. Following is the DMA analysis for PLA-based HDM composite.

DMA analysis for Tan delta versus temperature is shown in Fig. 16. The glass transition temperature of 10%, 20% and 30% are 71.32 °C, 70.41 °C, and 72.57 °C, all of which are higher far than neat PLA (64 °C) and even higher than neat epoxy (69.32 °C). The higher T_g than neat PLA presents significant chain mobilities, probably associated with the amorphous regions of PLA. However, the higher T_g than epoxy shows some significant intermolecular changes (reorientation or crystallization) that further point toward the formation of a proper composite. A similar nature of high strain is found for tensile samples. The noted intermolecular changes may be caused due to the high reaction temperature of epoxy and hardener with thin PLA walls in 10%, 20%, and 30%. The high temperature causes the adsorption of epoxy into the thin areas (area of fusion between PLA beads) [55]. The effect of adsorption

is also visible in form of distorted surface beads in Fig. 14. The adsorption at high temperature (> glass transition of PLA) further results in the reorientation of amorphous chains of PLA [56]. The two simultaneous phenomena, the adsorption (physical surface adhesion) and the intermolecular reorientation (chemical), result in the formation of a proper composite. The effects of the above-described chain reorientation are noted in form of highest strain as found in a flexural sample of 10% (Fig. 5). The high strain in flexure testing for 10% is also confirmed by strain vs temperature graphs of DMA (Fig. 16), in which 10% appears with one of the highest strain percentages.

Despite of the high glass transition temperature, the corresponding samples 10%, 20% and 30% show the least flexure strength (Fig. 5). In this regard, two types of DMA analysis are performed: 1) storage modulus vs temperature, and 2) stress vs temperature. As storage modulus present the overall stiffness of the material, the low storage modulus in Fig. 1 of each corresponding sample (10%, 20% and 30%) as compared to higher percentages (40% to 90%) justify the lowest flexure and tensile strength of the. Similarly in stress vs temperature graphs (Fig. 16), each corresponding sample (10%, 20%, and 30%) is observed with low stress as compared to the high percentages FFF samples (60% and 70). Therefore, based on the storage modulus and stress vs temperature analysis, the low strength of 10% to 30% is justified.

On the contrary, the samples of 50% to 90% have similar glass transition temperature as like 10% to 30% in Tan δ graphs (Fig. 15) but with high flexural strength (Fig. 5). This confusion is resolved with the high storage modulus of 50% to 90%. The high storage modulus justifies the high flexural strength of corresponding samples (50% to 90%). The storage modulus results are further supported by DMA graphs of stress vs temperature graphs (Fig. 16) that show high stress for 60% and 70% as compared to 10%, 20%, and 30%. Another reason for stability is found for 60% and 70% in strain vs temperature graphs. The 60% and 70% samples have pronounced cold crystallization peaks as compared to low percentage samples (10%, 20%, and 30%). The large area in the cold crystallization peak presents the increase in crystalline reorientation[57] that results in high stresses.

It is also noted that the glass transition temperature and storage modulus of 80% and 90% are lower than the 50%, 60%, and 70%. In this regard, the wall thickness of 80% and 90% are too thick to cause optimal adsorption of epoxy to form a proper composite. The low T_g and storage modulus present the comparative disadvantage of printing with the highest FFF percentages (80% and 90%). Hence, it justifies the value of this research work for achieving the optimal 3d-printed structure to save time and cost.
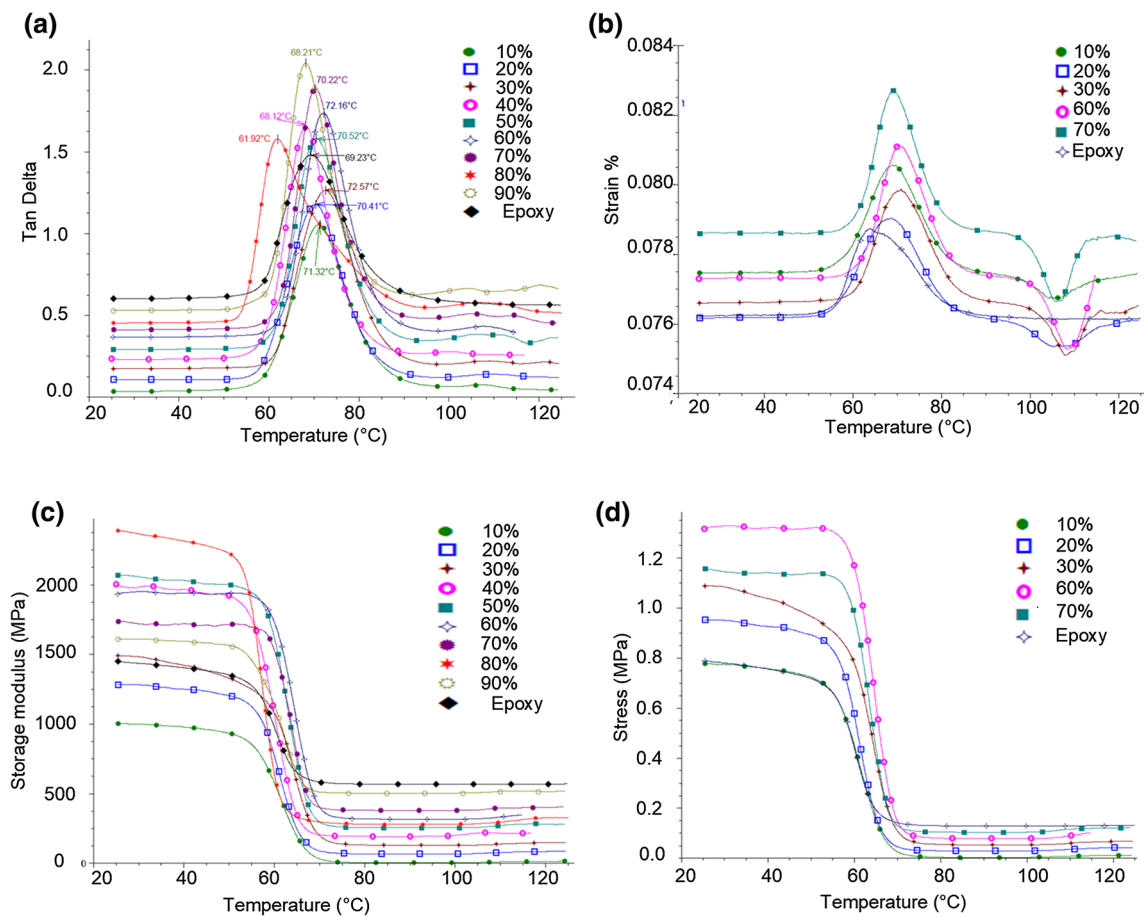
Fig. 16 DMA analysis of PLA/epoxy HDM composite for: **a** Tan delta versus temperature, **b** strain percentage versus temperature, **c** storage modulus versus temperature, and d) stress versus temperature

4.5 Future prospects

It is important to highlight the potential of manufacturing HDM composites as compared to pure FFF parts. The key benefits are associated with cost, and time. It is reported that time and cost are two key weaknesses of FFF that restrain its applications in various domains. HDM composite provides a best solution considering cost and time of 3D printing. As shown in Table 4 for tensile specimens, there is a significant decrease in cost of 3D-printed material (PLA) ranging from as high as ≈65% to ≈34%. Similarly, the 3D printing time is also decreased prominently ranging from 50 to 20%. The future prospect of utilizing HDM composite technique instead of 100% FFF is further strengthen with superior mechanical properties depending on 3D printing material.

However, as evident form ABS-based HDM composites, this research work related to HDM composite technique is in its early stages and limited to types of 3D printing materials (PLA). Therefore, it requires a thorough research in future to explore ways to utilize full potential of HDM compositing.

5 Conclusion

The research presents a complete range of volume distributions between FFF structures filled with a two-part epoxy system for tensile, compressive, and flexure characterizations. It includes in situ image analysis, SEM, and DMA for analyzing the overall stability and fracture mechanics of the HDM composites. Following results are concluded,

- 70% and 80% are the most optimal for tensile analysis of PLA/epoxy HDM composite with good tensile stress of about 62 MPa.
- 70%, 80%, and 90% are the most optimal for compressive analysis of PLA/epoxy HDM composite with good strength (≈50 MPa) and minimum strain.
- 60%, 70%, 80% and 90% are the most optimal for flexure analysis of PLA/epoxy HDM composite with higher stress (≥ 109 MPa) than neat PLA.
- The 70% and 80% PLA compositions as optimal FFF percentages achieves better properties due to replacement of 30% and 20% void-based structure with void-

Table 4 Comparison of cost and time for 3D printing performed in HDM with 100% FFF

Part (%)	Weight (g)	Length of filament (m)	Cost of filament		Cost of used filament (USD)	Difference in cost (USD)	Percentage difference in cost (%)	Time for 3D printing only		
			1000 g (USD)	1 g (USD)				Time for FFF (min)	Difference in time (min)	Percentage difference in time (%)
20	1.97	0.66	29.9	0.0299	0.059	−0.109	−64.884	15	−15.000	−50.000
30	2.07	0.69	29.9	0.0299	0.062	−0.106	−63.102	17	−13.000	−43.333
40	2.68	0.90	29.9	0.0299	0.080	−0.088	−52.228	18	−12.000	−40.000
50	2.72	0.91	29.9	0.0299	0.081	−0.086	−51.515	22	−8.000	−26.667
60	3.34	1.12	29.9	0.0299	0.100	−0.068	−40.463	23	−7.000	−23.333
70	3.39	1.14	29.9	0.0299	0.101	−0.066	−39.572	20	−10.000	−33.333
80	3.7	1.24	29.9	0.0299	0.111	−0.057	−34.046	24	−6.000	−20.000
100	5.61	1.88	29.9	0.0299	0.168	0.000	0.000	30	0.000	0.000

less-filled epoxy, respectively. This results in less FFF material, low cost, less printing time.

- ABS does not show proper adhesion with filled epoxy and thus fracture early in all characterization testing.
- DMA reveals the two simultaneous phenomenon to be the reason of superior properties in PLA/epoxy HDM composites. i.e., adsorption at high reaction temperature of epoxy and high intermolecular re-orientation that increases the crystallinity of PLA.
- Future prospect of HDM compositing, subject to limitation of material (PLA), is justified with the ≈65% to ≈34% decrease in cost and 50% to 20% decrease in time as compared to 100% FFF.

Declarations

References

1. Solomon IJ, Sevvel P, Gunasekaran J (2020) A review on the various processing parameters in FDM. Mater Today: Proc 37:509–515. https://doi.org/10.1016/j.matpr.2020.05.484

2. Mazurchevici AD, Nedelcu D, Popa R (2020) Additive manufacturing of composite materials by FDM technology: a review. Indian J Eng Mater Sci

3. de Oliveira TL, de Carvalho J (2021) Design and numerical evaluation of quadrotor drone frame suitable for fabrication using fused filament fabrication with consumer-grade ABS. J Braz Soc Mech Sci Eng 43(9):1–19

4. Dave HK, Patel BH, Rajpurohit SR, Prajapati AR, Nedelcu D (2021) Effect of multi-infill patterns on tensile behavior of FDM printed parts. J Braz Soc Mech Sci Eng 43(1):1–15

5. Anoop M, Senthil P, Sooraj V (2021) An investigation on viscoelastic characteristics of 3D-printed FDM components using RVE numerical analysis. J Braz Soc Mech Sci Eng 43(1):1–13

6. Wu X et al (2022) Cellulose nanocrystals-mediated phase morphology of PLLA/TPU blends for 3D printing. Chin J Polym Sci 40:1–11

7. Korkut V, Yavuz H (2020) Enhancing the tensile properties with minimal mass variation by revealing the effects of parameters in fused filament fabrication process. J Braz Soc Mech Sci Eng 42(10):1–18

8. Whyman S, Arif KM, Potgieter J (2018) Design and development of an extrusion system for 3D printing biopolymer pellets. Int J Adv Manuf 96(9–12):3417–3428

9. Duty CE et al (2017) Structure and mechanical behavior of Big area additive manufacturing (BAAM) materials. Rapid Prototyp J 23:181–189. https://doi.org/10.1108/RPJ-12-2015-0183

10. Duty CE, Drye T, Franc A (2015) Material development for tooling applications using big area additive manufacturing (BAAM). Oak Ridge National Lab (ORNL), Oak Ridge, TN (United States). Manufacturing

11. Ajinjeru C et al (2016) The influence of rheology on melt processing conditions of amorphous thermoplastics for big area additive manufacturing (BAAM). Solid Freeform Fabr 2016:754–761

12. Ajinjeru C et al (2018) The influence of dynamic rheological properties on carbon fiber-reinforced polyetherimide for large-scale extrusion-based additive manufacturing. Int J Adv Manuf 99(1):411–418. https://doi.org/10.1007/s00170-018-2510-z

13. Ajinjeru C et al (2019) Rheological survey of carbon fiber-reinforced high-temperature thermoplastics for big area additive manufacturing tooling applications. J Thermoplast Compos Mater 34:1443–1461. https://doi.org/10.1177/0892705719873941

14. Ajinjeru C et al (2017) The influence of rheology on melt processing conditions of carbon fiber reinforced polyetherimide for big area additive manufacturing. Oak Ridge National Lab (ORNL), Oak Ridge

15. Zhang H, Huang T, Jiang Q, He L, Bismarck A, Hu Q (2021) Recent progress of 3D printed continuous fiber reinforced polymer composites based on fused deposition modeling: a review. J Mater Sci 56(23):12999–13022

16. Lalegani Dezaki M, Mohd Ariffin MKA (2020) The effects of combined infill patterns on mechanical properties in FDM process. Polymers 12(12):2792. https://doi.org/10.3390/polym12122792

17. Farashi S, Vafaee F (2022) Effect of printing parameters on the tensile strength of FDM 3D samples: a meta-analysis focusing on layer thickness and sample orientation. Progress in Additive Manufacturing, pp 1–18

18. Wang J et al (2019) Morphology evolutions and mechanical properties of in situ fibrillar polylactic acid/thermoplastic polyurethane blends fabricated by fused deposition modeling. Macromol Mater Eng 304(7):1900107. https://doi.org/10.1002/mame.201900107

19. Raspopina V, Perelygina A, Shemetov L, Grigorov P (2022) Dependence between the mechanical characteristics of the material and the FDM sample made from this material. In: Safety in aviation and space technologies. Springer, pp 215–227

20. Sharma R, Singh R, Penna R, Fraternali F (2018) Investigations for mechanical properties of Hap, PVC and PP based 3D porous structures obtained through biocompatible FDM filaments. Compos B Eng 132:237–243

21. Alafaghani AA, Qattawi A, Alrawi B, Guzman A (2017) Experimental optimization of fused deposition modelling processing parameters: a design-for-manufacturing approach. Procedia Manuf 10:791–803. https://doi.org/10.1016/j.promfg.2017.07.079

22. Vaezi M, Yang S (2015) Extrusion-based additive manufacturing of PEEK for biomedical applications. Virtu Phys Protot 10(3):123–135

23. Pandžić A, Hodžić D, Kadrić E (2021) Experimental investigation on influence of infill density on tensile mechanical properties of different FDM 3D printed materials. Parameters 3:4

24. Obeid S, Madžarević M, Krkobabić M, Ibrić S (2021) Predicting drug release from diazepam FDM printed tablets using deep learning approach: Influence of process parameters and tablet surface/volume ratio. Int J Pharm 601:120507

25. Kumar KS, Soundararajan R, Shanthosh G, Saravanakumar P, Ratteesh M (2021) Augmenting effect of infill density and annealing on mechanical properties of PETG and CFPETG composites fabricated by FDM. Mater Today: Proc 45:2186–2191

26. Nazir A, Abate KM, Kumar A, Jeng J-Y (2019) A state-of-the-art review on types, design, optimization, and additive manufacturing of cellular structures. Int J Adv Manuf Technol 104(9):3489–3510

27. Rezaie R, Badrossamay M, Ghaie A, Moosavi H (2013) Topology optimization for fused deposition modeling process. Procedia Cirp 6:521–526

28. Mellal MA, Laifaoui C, Ghezal F, Williams EJ (2022) Multi-objective factors optimization in fused deposition modelling with particle swarm optimization and differential evolution. Int J Interact Design Manuf (IJIDeM) 1–6

29. Paul S (2021) Finite element analysis in fused deposition modeling research: A literature review. Measurement 178:109320

30. Dev S, Srivastava R (2021) Effect of infill parameters on material sustainability and mechanical properties in fused deposition modelling process: a case study. Prog Addit Manuf 6(4):631–642

31. Brenken B, Barocio E, Favaloro A, Kunc V, Pipes RB (2018) Fused filament fabrication of fiber-reinforced polymers: a review. Addit Manuf 21:1–16

32. Al-Maharma AY, Patil SP, Markert B (2020) Effects of porosity on the mechanical properties of additively manufactured components: a critical review. Mater Res Express 7(12):122001

33. Awasthi P, Banerjee SS (2021) Fused deposition modeling of thermoplastics elastomeric materials: challenges and opportunities. Addit Manuf 46:102177. https://doi.org/10.1016/j.addma.2021.102177

34. Behzadnasab M, Yousefi AA, Ebrahimibagha D, Nasiri F (2019) Effects of processing conditions on mechanical properties of PLA printed parts. Rapid Prototyp J

35. Popescu D, Zapciu A, Amza C, Baciu F, Marinescu R (2018) FDM process parameters influence over the mechanical properties of polymer specimens: a review. Polym Testing 69:157–166

36. Pernica J, Sustr M, Dostal P, Brabec M, Dobrocky D (2021) Tensile testing of 3D printed materials made by different temperature. Manuf Technol 21(3):398–404

37. "Mechanical properties of direct waste printing of polylactic acid with universal pellets extruder: comparison to fused filament fabrication on open-source desktop three-dimensional printers". 3D

Print Addit Manuf 7(5):237–247. https://doi.org/10.1089/3dp.2019.0195

38. Chueh Y-H, Zhang X, Ke JC-R, Li Q, Wei C, Lin L (2020) Additive manufacturing of hybrid metal/polymer objects via multiple-material laser powder bed fusion. Addit Manuf 36:101465. https://doi.org/10.1016/j.addma.2020.101465

39. Zhu Z, Dhokia V, Nassehi A, Newman ST (2016) Investigation of part distortions as a result of hybrid manufacturing. Robot Comput Integr Manuf 37:23–32. https://doi.org/10.1016/j.rcim.2015.06.001

40. Belter JT, Dollar AM (2014) Strengthening of 3D printed robotic parts via fill compositing. In: Presented at the 2014 IEEE/RSJ international conference on intelligence robotics system, Chicago, September 14–18, p 14718047

41. Ma RR, Belter JT, Dollar AM (2015) Hybrid deposition manufacturing: design strategies for multimaterial mechanisms via three-dimensional printing and material deposition. J Mech Robot 7(2):021002. https://doi.org/10.1115/1.4029400

42. Wittbrodt B, Pearce JM (2015) The effects of PLA color on material properties of 3-D printed components. Addit Manuf 8:110–116

43. ASTM. "D638-14, Standard Test Method for Tensile Properties of Plastics." ASTM International. https://www.astm.org/Standards/D638. Accessed 01 Jan 2021

44. Auffray L, Gouge P-A, Hattali L (2021) Design of experiment analysis on tensile properties of PLA samples produced by fused filament fabrication. Int J Adv Manuf Technol 1–15

45. ISO. "ISO 178:2019 Plastics-Determination of flexural properties." https://www.iso.org/standard/70513.html. Accessed 01 Jan 2021

46. ISO. "ISO 604:2002 Plastics-Determination of compressive properties." https://www.iso.org/standard/31261.html. Accessed 01 Jan 2021

47. Anitha R, Arunachalam S, Radhakrishnan P (2001) Critical parameters influencing the quality of prototypes in fused deposition modelling. J Mater Process Technol 118(1):385–388. https://doi.org/10.1016/S0924-0136(01)00980-3

48. Song Y, Li Y, Song W, Yee K, Lee K-Y, Tagarielli VL (2017) Measurements of the mechanical response of unidirectional 3D-printed PLA. Mater Des 123:154–164

49. von Windheim N, Collinson DW, Lau T, Brinson LC, Gall K (2021) The influence of porosity, crystallinity and interlayer adhesion on the tensile strength of 3D printed polylactic acid (PLA). Rapid Prototyp J

50. Yadav P, Sahai A, Sharma RS (2021) Strength and surface characteristics of FDM-based 3D printed PLA parts for multiple infill design patterns. J Inst Eng (India): Ser C 102(1):197–207

51. Abbas T, Othman FM, Ali HB (2017) Effect of infill Parameter on compression property in FDM Process. Dimensions 12(7):25–4

52. Othman FM, Fadhil T, Ali AHB (2018) Influence of process parameters on mechanical properties and printing time of FDM PLA printed parts using design of experiment. J Eng Res 2248–9622

53. Ranney TA, Parker LV (1995) Susceptibility of ABS, FEP, FRE, FRP, PTFE, and PVC well casings to degradation by chemicals. Cold Regions Research and Engineering Lab Hanover NH

54. Ranney TA, Parker LV (1997) Comparison of fiberglass and other polymeric well casings, part I: susceptibility to degradation by chemicals. Groundw Monit Remed 17(1):97–103

55. Nuthong W, Uawongsuwan P, Pivsa-Art W, Hamada H (2013) Impact property of flexible epoxy treated natural fiber reinforced PLA composites. Energy Procedia 34:839–847. https://doi.org/10.1016/j.egypro.2013.06.820

56. Harris M, Potgieter J, Archer R, Arif KM (2019) In-process thermal treatment of polylactic acid in fused deposition modelling. Mater Manuf Processes 34(6):701–713

57. Mofokeng JP, Luyt A, Tábi T, Kovács J (2012) Comparison of injection moulded, natural fibre-reinforced composites with PP and PLA as matrices. J Thermoplast Compos Mater 25(8):927–948. https://doi.org/10.1177/0892705711423291

Hybrid deposition additive manufacturing: novel volume distribution, thermo-mechanical characterization, and image analysis

Harris, M

2022-08-25